Emergence of layered nanoscale mesh networks through intrinsic molecular confinement self-assembly

Zehao Sun,[1†] Runze Liu,[1†] Tingyu Su,[2] Hejin Huang,[1] Ken Kawamoto,[3] Ruiqi Liang,[4] Bin Liu,[3] Mingjiang Zhong,[4] Alfredo Alexander-Katz,[1] Caroline A. Ross,[1*] Jeremiah A. Johnson[1,3*]

Affiliations

[1]Department of Materials Science and Engineering, Massachusetts Institute of Technology, 77 Massachusetts Avenue, Cambridge, MA 02139, U.S.A.

[2]Department of Mechanical Engineering, Massachusetts Institute of Technology, 77 Massachusetts Avenue, Cambridge, MA 02139, U.S.A.

[3]Department of Chemistry, Massachusetts Institute of Technology, 77 Massachusetts Avenue, Cambridge, MA 02139, U.S.A.

[4]Department of Chemical and Environmental Engineering, Yale University, 225 Prospect Street, New Haven, CT 06520, U.S.A.

[†]These authors contributed equally to this work.

[*]Correspondence to caross@mit.edu (C.A.R); jaj2109@mit.edu (J.A.J.)

Abstract

Block copolymer self-assembly is a powerful tool for 2D nanofabrication; however, its extension to complex 3D network structures, which would be useful for a range of applications, is limited. Here, we report a simple method to generate unprecedented 3D mesh morphologies through intrinsic molecular confinement self-assembly. We designed triblock bottlebrush polymers with two Janus domains: one perpendicular and one parallel to the polymer backbone. The former enforces a lamellar superstructure that intrinsically confines the intra-layer self-assembly of the latter, giving rise to a mesh-like monoclinic M^{15} network substructure with excellent long-range order. Dissipative particle dynamics simulations show that the spatial constraints exerted on the polymer backbone drive the emergence of M^{15}, as well as a tetragonal T^{131} in the strong segregation regime. This work demonstrates intrinsic molecular confinement as a path to bottom-up assembly of new geometrical phases of soft matter, extending the capabilities of block copolymer nanofabrication.

Main text

Classical block copolymer self-assembly enables access to a range of well-known, useful, but limited, ordered nanostructure geometries, such as spheres, cylinders (CYL), gyroids (GYR), and lamellae (LAM)[1–5]. Nevertheless, there remains a large gap between the simple patterns commonly formed by block copolymers and the patterns required for many nanoscale applications. For example, single- and multilayer mesh nanostructures, which are defined as overlaid parallel lines with different orientations (Fig. 1f), are of particular interest in a range of technologies, such as photonic materials, superhydrophobic coatings, flexible electronics, and cross-point devices[6–10]; their fabrication, however, has been a long-standing challenge. For single-layer nanomeshes, state-of-the-art techniques include successive shear or laser alignment of two CYL layers[11,12] as well as directed self-assembly of CYL or LAM layers on topographically-patterned substrates with post arrays or trenches[7,8,13,14]; for multilayer nanomeshes, all current techniques require repetitive layer-by-layer overlay steps[7,15,16]. Thus far, a simple, straightforward fabrication process through "bottom-up" macromolecular design rather than "top-down" pre- or post-treatments has not been demonstrated.

Addressing this challenge is no easy task: Conventional block copolymer phase diagrams offer few opportunities for the formation of ordered 3D continuous network phases. Without constraints in any direction in space, unconfined microphase separation tends to give cubic-symmetric networks, among which GYR is most frequently observed, though rarer diamond and primitive cubic have also been reported[17,18]. The only exception among the reported equilibrium network phases is O^{70} (orthorhombic *Fddd*, space group 70) as a single-network of relatively low symmetry[19–21] (Supplementary Figs. 4a and 5a), but its phase region is narrow because its formation is associated with the instability of the GYR phase at the GYR/CYL boundary in the weak segregation limit[22]. Its derivative structure, O^{52} (*Pnna*), was reported as a non-equilibrium phase stabilized by shear[23,24].

Given that mesh structures are anisotropic networks, their formation requires symmetry breaking. We gained inspiration from our previous studies on directed self-assembly, where nanoscale topographical constraints yield emergent symmetries[8,25], and considered whether analogous confinement could be achieved *intrinsically* via (macro)molecular design, noting that the study of low-symmetry network phases under confinement at the molecular level remains unexplored. Although non-network, comparatively simple nesting X-in-Y (X, Y = LAM, CYL, *etc*.) morphologies have long been predicted and observed for linear ABC terpolymers[26,27], the inability to decouple the substructure (X) and superstructure (Y) formation greatly complicates the exploration of a large parameter space.

Here, we introduce a new "intrinsic molecular confinement" (IMC) self-assembly strategy that overcomes these challenges. Using our multiblock Janus bottlebrush copolymer (JBBC)[5,28,29] architectures, we achieve multilayer nanomesh structures wherein hierarchical X-in-Y self-assembly gives microphase-separated sub- and superstructures (Fig. 1a), each of which can be independently tuned. Using a suite of experimental

characterization methods and dissipative particle dynamics (DPD) simulations, we show that roughly in the same phase region as the GYR structure produced by unconfined self-assembly, IMC provides access to a mesh-like low-symmetry network with a 54° included angle that proved to be an unprecedented M^{15} phase (monoclinic *C*2/*c*, space group 15, Fig. 1b,c) not reported before in soft materials. Moreover, the IMC self-assembly approach (Fig. 1c–e) can produce large-scale, highly-ordered single- or multilayer M^{15}-in-LAM patterns on bare silicon substrates through a simple solvent annealing step, without the need for specialized substrates[12] or low-throughput templating techniques such as electron-beam lithography[30,31]. Finally, a metastable network substructure, which is yet another mesh-like network but with a 90° included angle and tetragonal symmetry, was achieved experimentally using ICM; it was predicted to be stable in the strong segregation regime by DPD simulations and identified as T^{131} (tetragonal $P4_2/mmc$, space group 131). These results pioneer ICM self-assembly as a new concept for the fabrication of complex soft materials.

Molecular design and synthesis of triblock JBBCPs

Triblock JBBCPs with the general formula $(A_x\text{-}branch\text{-}B_y)_n\text{-}block\text{-}(C_z)_m$, where A = polydimethylsiloxane (PDMS) with number-average molar mass (M_n) of x = 5.0 kg mol^{-1}, B = polystyrene (PS) with varied M_n (y), and C = poly(lactic acid) (PLA) with M_n of z = 6.3 kg mol^{-1}; and m and n are the number-average degrees of polymerization (DPs) of the A-*branch*-B and C domains, respectively, were synthesized and characterized (see Supplementary Information for full synthetic details). These JBBCPs are designed such that a substructure forms through microphase separation of A and B normal to the JBBCP backbone, which is intrinsically confined by a superstructure formed from microphase separation of the A-*branch*-B domains from the C domain (Fig. 1a). Larger side chain M_n values compared to previously reported triblock JBBCPs[29] were targeted to (i) facilitate access to the network phase region by finer control over the volume fractions; (ii) obtain larger feature sizes (~ 10^1 nm, the resolution limit of electron microscopy for polymer materials), which can facilitate direct imaging characterization; and (iii) drive stronger microphase separation, which provides a wider window for annealing while avoiding order-disorder transitions[32]. The substructure morphology was explored by varying the volume fraction of A in the A-*branch*-B domain (f_A') from 0.3 to 0.5, which was achieved using y = 4.6, 6.9, 8.2, 9.2, and 10.3 kg mol^{-1}. The effect of the superstructure, which confines the substructure, was examined by varying m and n. A complete list of the synthesized triblock JBBCPs is provided in Supplementary Table 1. For simplicity, we refer to these samples as **T*y*$_{m\text{-}n}$**, where "**T**" represents triblock, the following digits indicate the M_n of B (in the unit of kg mol^{-1}), and the subscript indicates the backbone DPs. For example, **T6.9$_{50\text{-}20}$** has the following composition: $(PDMS_{5.0\ kg\ mol^{-1}}\text{-}branch\text{-}PS_{6.9\ kg\ mol^{-1}})_{20}\text{-}block\text{-}(PLA_{6.3\ kg\ mol^{-1}})_{50}$.

Single layer and multilayer nanomesh pattern formation

With these samples in hand, IMC self-assembly was investigated following the fabrication steps outlined in Fig. 1f, with results from **T6.9$_{30\text{-}30}$** described here as an exemplar. First, a

thin film of **T6.9$_{30\text{-}30}$** was spin-coated onto a silicon substrate grafted with a C-homopolymer brush, the latter of which is required to orient the JBBCP superstructure parallel to the substrate by removing surface diffusion barriers[33] and lowering the surface energy of the C domain[34]. Without this surface functionalization, the orientation of the superstructure was poorly controlled (Supplementary Fig. 17b). Next, gradient solvent annealing in chloroform vapor was performed to promote IMC self-assembly (Fig. 1c–e), where the swelling ratio of the film was controlled by nitrogen flow in a reservoir system[35]. The films were subjected to a high degree of swelling for 30 min to anneal and orient the confining superstructure, which was observed by scanning electron microscopy (SEM) to be horizontal LAM, as expected (Supplementary Fig. 17e). In the course of this process, we noticed an unusual mesh network substructure, but it did not display long-range order due to the weak segregation of the A and B domains under these conditions[36] (Supplementary Fig. 17c). Thus, to further drive assembly of this substructure, we exposed the sample to subsequent reduced swelling annealing conditions for various times. Strikingly, this process produced reasonably ordered mesh substructures within 5 min (Supplementary Fig. 20), which improved further as the annealing time increased (Supplementary Fig. 17d). Ultimately, micron-scale ordered mesh network grains were obtained after 2 hours (Fig. 2a and Supplementary Fig. 21). Reactive ion etching (RIE, see Methods for details) was used to remove the B and C (PS and PLA, respectively) domains and retain the mesh-forming A block by oxidizing the PDMS[33]. Fast Fourier transform (FFT) of the top-view SEM images of films prepared from **T6.9$_{30\text{-}30}$** (Fig. 2a inset) revealed a mesh network pattern with an included angle of 54° and a line spacing of 17.5 nm. This simple and spontaneous formation of well-ordered meshes separated by superstructure layers contrasts with the sequential multi-step overlay methods used previously to form nanoscale mesh structures[7,13,15,16].

Given that the super- and substructure formation are independently controlled in this system, the number of mesh-patterned layers, *i.e.*, the number of horizontal lamellae of the superstructure, can be arbitrarily tuned by simply adjusting the spin-coated film thickness. Examples of the formation of single- to 4-layer nanomesh patterns, as evidenced by cross-sectional views, are shown in Fig. 2d–g. The number of layers can keep increasing as needed (Supplementary Figs. 32–33), though micron-scale thick films require longer annealing time (around 4 hours in total). Remarkably, even a multilayer mesh pattern with as many as 50 layers could be easily fabricated using this method (Fig. 2h and Supplementary Fig. 31), a daunting task by any other nanofabrication technique.

For multilayer nanomeshes, angled etching was employed to create terraces on the thin film surface[37], confirming that the mesh was present in the lower layers (Fig. 2c). High power CF_4/O_2 RIE reveals the internal morphology[38] (Supplementary Fig. 34). Cross-sectional SEM images (Fig. 2i–k) show patterns characteristic of the M^{15} network structure (Fig. 2l–n) throughout the film.

Identification of the M^{15} network structure

We identified the mesh-like substructure as an undiscovered low-symmetry monoclinic M^{15} network phase (M for monoclinic; space group 15 or $C2/c$), despite its cuboidal unit cell (Fig. 1b,c; see Supplementary Data 1 for 3D models). Though M^{15} shares some similarities with the reported orthorhombic O^{70} *Fddd* phase[19–22] in terms of its network connectivity and the appearance of certain projections (Supplementary Figs. 4–5; see Supplementary Information for more details), M^{15} and O^{70} show disparate symmetries and phase behaviors, described below. One way of visualizing the complex network structure is to view it as ABA-stacked layers of parallel lines that are twisted at an angle (Supplementary Fig. 6a). This organization is evident from the top surface of the cross-sectional SEM images, which display unidirectional parallel line patterns (Fig. 2d–h). Notably, these lines are not straight, but rather wavy in the out-of-plane direction (*i.e.*, the *c* axis of the lattice), forming hexagonally packed round holes as observed from the side (Fig. 2k,n). The "twist angle", or the included angle θ of the nanomesh, is dictated by the ratio of the lattice parameters *a* and *b,* with $\theta = 2\arctan(a/b)$. Free energy arguments analogous to those made for O^{70} phase stability[22] as well as our DPD simulations (Supplementary Fig. 43) suggest a preferential ratio of $a : b = 1 : 2$, in good accordance with the 54° angle observed in experiments (Fig. 2a). The mesh-like (001) plane of the M^{15} substructure was found to be exclusively parallel to the LAM superstructure (Supplementary Fig. 17b,d), likely due to the polymer backbone configuration at the interface with the C domain (see discussion in the next section), but the in-plane orientation of the M^{15} substructure was random, resulting in grains with various appearances in cross-section (Fig. 2i–k).

Unfortunately, analysis of the network substructure through scattering or diffraction techniques is not possible, as the substructure is not 3D-periodic but sandwiched and confined by the LAM superstructure without interlayer correlations (Fig. 2c and Supplementary Fig. 44). This "slicing effect" is clearly observed in the FFT of a simulated M^{15}-in-LAM structure, showing severe peak broadening and loss of information when compared to that of a bulk M^{15} structure (Supplementary Fig. 25). Indeed, peak broadening was observed in the experimental small-angle X-ray scattering (SAXS) profile of the solvent annealed $\mathbf{T6.9_{30\text{-}30}}$ sample (Supplementary Fig. 48). Therefore, direct imaging techniques were necessary to characterize the network substructure.

The top (Fig. 2a) and cross-sectional view (Fig. 2i-k) SEM images show qualitative agreement with the [001], [1$\bar{1}$0], [110], and [100] projections of the M^{15} model (Fig. 2a inset and Fig. 2l-n). A tilted view is shown in Supplementary Fig. 26. Although RIE slightly reduces the out-of-plane dimensions, we have previously found that etched samples provide a high-fidelity rendition of the original microdomain features[39]. Nevertheless, as a comparison, unetched thin-film samples were sectioned by a focused ion beam (FIB) and imaged by high-angle annular dark-field scanning transmission electron microscopy (HAADF-STEM), showing clearer but similar cross-sectional patterns (Fig. 3a and Supplementary Figs. 28–29) *vs* SEM. STEM imaging of unetched single-layer nanomeshes fabricated on a silicon nitride membrane substrate exhibited a top view that was similar to the SEM images (Fig. 3h), though the interpretation of the STEM projections is less

straightforward (see discussion in Supplementary Figs. 29–30). 3D tomography measurements of the sample of Fig. 3a elucidate the structural features (Supplementary Video 1). The reciprocal space pattern of the substructure clearly confirms its monoclinic symmetry (Supplementary Fig. 24g–i), and the reconstructed real space 3D geometry (Fig. 3b–d and Supplementary Video 2) closely resemble the mathematical model of the M^{15} substructure (Fig. 3e–g and Supplementary Video 2).

A possible mechanism for M^{15} phase formation

We hypothesized that the M^{15} substructure and its preferential interfacial (001) orientation formed in the A-*branch*-B domain are uniquely made possible through IMC imposed by the C domain and the resulting superstructure. To test this hypothesis, we synthesized an A-*branch*-B diblock JBBCP[5] ($PDMS_{5.0\,kg\,mol^{-1}}$-*branch*-$PS_{6.9\,kg\,mol^{-1}}$)$_{30}$ (**D6.9$_{30}$**) with the same chemical composition as the A-*branch*-B domain of **T6.9$_{30\text{-}30}$** and solvent-annealed this polymer under the same conditions as **T6.9$_{30\text{-}30}$**. Remarkably, this diblock JBBCP forms a cubic symmetric GYR morphology instead of M^{15} (Fig. 4a,b), strongly supporting our hypothesis.

This difference—M^{15} morphology for an intrinsically confined triblock JBBCP *vs* GYR an unconfined diblock variant—was explored further using a reparametrized DPD model[40] (see Methods for details). With a sensible choice of the modelling parameters, we were able to reproduce the GYR (Fig. 4c–e) and M^{15}-in-LAM morphologies (Fig. 4g–j and Supplementary Figs. 43–44) of diblock and triblock JBBCPs respectively, supporting our experimental interpretation. The DPD model was also successful in explaining the non-uniform thicknesses of the LAM superstructure for the triblock (Fig. 3a) with incommensurate height restrictions, *i.e.*, when the total thickness is not exactly an integer multiple of the equilibrium LAM spacing (Supplementary Fig. 51).

As a particle-based approach, the DPD model offers insights into the geometry of individual polymer chains. Interestingly, the backbones of the simulated GYR-forming diblock JBBCP were found to be rather more coiled at the 3-way nodes (Fig. 4e) than in the interconnecting struts (Fig. 4d), similar to a previous conclusion from the simulation of linear diblock copolymers known as "packing frustration"[41]. For the corresponding triblock JBBCP with the same A to B volume ratio (*i.e.*, f_A(diblock) = f_A'(triblock)), the presence of the LAM superstructure requires that the ends of the backbones in the A-*branch*-B domain must be pinned at the interface, making it difficult for these backbones to bend to accommodate the node structure. As a result, this IMC results in a more extended configuration of the backbones for the triblock JBBCPs (Fig. 4h–j and Supplementary Fig. 50) and globally stabilizes the M^{15} phase over GYR. These results reflect a strong effect of the molecular-level backbone geometry on the final mesoscale morphology: coiled backbones produce a more curved GYR morphology, whereas rigid, extended backbones create sharper junctions and give rise to a M^{15} phase with straighter network struts.

The phase diagrams of diblock and triblock JBBCPs

To identify the phase region for the M^{15} structure, the IMC self-assembly of triblock JBBCPs with different f_A' and backbone DPs (*i.e.*, *m* and *n*) were compared with the

corresponding unconfined diblock JBBCPs **D*y*$_n$** (a diblock with B branch M_n of y kg mol^{-1} and a backbone DP of n). A complete list of tested samples is shown in Supplementary Table 1. For all m and n tested, the observed superstructures for triblock JBBCPs were LAM due to the rigidity of the poly(norbornene) backbone[4]; the backbone DP had little impact on the final morphologies (Supplementary Figs. 37–39), in accordance with previous observations[5,29].

Next, the morphology as a function of the volume fraction f_A(diblock) or f_A'(triblock) was studied (Supplementary Figs. 36–40); the results are summarized in Fig. 4f. The effective volume fraction in a swelled film varies with the solvent annealing condition; therefore, a qualitative model[42] was applied to account for this effect (see Supplementary Information). The experimental and simulated (Supplementary Figs. 41–42) phase diagrams match remarkably well with each other (Fig. 4f), indicating that the phase behavior can be generalized for different chemical blocks. More importantly, both show a one-to-one mapping between diblock and triblock phase regions. For the triblock JBBCP discussed in this paper, the M^{15} substructure phase emerges at an effective f_A' of 32% and ends at ~39%, conforming well to the GYR phase region of the diblock JBBCP. Those polymers with $f_A' < 32\%$ or $> 39\%$ showed CYL-in-LAM or LAM-in-LAM hierarchical morphologies respectively (Supplementary Figs 40 and 36), as reported elsewhere[29]. It is noteworthy that the M^{15} phase region is wide and overlapping with the GYR phase region, which is fundamentally different from previously reported network phases, such as O^{70}, that have narrow windows of stability and border the GYR phase. This finding suggests that IMC self-assembly can literally replace a known phase of the classical block copolymer phase diagram with a new phase.

The above studies utilized solvent annealing, and we found that thermal annealing yielded qualitatively similar trends (Supplementary Figs 45–47) but with poorer order and sometimes mixed morphologies. An interesting phenomenon observed for both solvent and thermally annealed M^{15}-in-LAM-forming samples, however, was the coexistence of the 54° mesh network (from the M^{15} substructure) alongside a small fraction of a 90° mesh network (Fig. 2b and Supplementary Figs. 22, 55 and 56). A detailed structural analysis was not possible given its rare occurrence. However, we managed to capture a similar intermediate state in the DPD model during its evolution (Supplementary Fig. 52), indicating that it represents a metastable phase. This new tetragonal T^{131} ($P4_2/mmc$, space group 131) structure has a distinct network connectivity compared to M^{15} (Supplementary Figs. 4, 6, and 53; Supplementary Information) and can be described by a Schwarz CLP minimal surface (also known as “crossed layers of parallels”). Furthermore, our DPD model predicts a more energetically favorable T^{131} substructure than M^{15} if the interaction parameter χN is greater than a critical value (Supplementary Fig. 54), suggesting that T^{131} might be promoted experimentally under higher segregation conditions. Indeed, we observed a larger fraction of T^{131} after thermal annealing (Supplementary Fig. 56), where the effective χ is larger without the interaction-screening solvent molecules[42].

The calculation of free energies under different interaction parameters in DPD simulations also provides another viewpoint on the rationalization of the emergence of

these network phases in triblock JBBCPs. Although an M^{15} or T^{131} network could be obtained in simulations using the diblock architecture (Supplementary Fig. 53), due to the existence of a low-energy GYR phase, they could not be stabilized unless an unusually high χN is set; consequently, they are completely missing in experiments. In contrast, the IMC-induced destabilization of GYR in the triblock JBBCPs allows the formation of these high-energy phases.

Conclusion

We present the self-assembly of triblock JBBCPs, achieving for the first time the formation of a highly-ordered multilayer (1- to 50-layer) mesh pattern on a flat silicon substrate in a simple process. The mesh substructure is a novel monoclinic M^{15} network phase, and forms over a relatively wide compositional window, which roughly matches the GYR phase region for diblock JBBCPs. Simulations reveal that the stabilization of this low-symmetry network phase is due to the restrictions imposed on the geometry of the backbone at the interfaces with the lamellar superstructure. This work not only provides a simple solution for a fabrication challenge that could facilitate manufacturing of nanoscale devices, but also sheds light on the physics behind intrinsically confined self-assembly of block copolymers, promising a path to the discovery of other new network phases in soft matter systems.

References

1. Bates, F. S. & Fredrickson, G. H. Block copolymers—designer soft materials. *Phys. Today* **52**, 32–38 (1999).
2. Hamley, I. W. Nanostructure fabrication using block copolymers. *Nanotechnology* **14**, R39–R54 (2003).
3. Segalman, R. A. Patterning with block copolymer thin films. *Mater. Sci. Eng. R Rep.* **48**, 191–226 (2005).
4. Bolton, J., Bailey, T. S. & Rzayev, J. Large pore size nanoporous materials from the self-assembly of asymmetric bottlebrush block copolymers. *Nano Lett.* **11**, 998–1001 (2011).
5. Kawamoto, K. *et al.* Graft-through synthesis and assembly of Janus bottlebrush polymers from A-*branch*-B diblock macromonomers. *J. Am. Chem. Soc.* **138**, 11501–11504 (2016).
6. Cheng, L.-C. *et al.* Imparting superhydrophobicity with a hierarchical block copolymer coating. *Small* **16**, 1905509 (2020).
7. Tavakkoli K. G., A. *et al.* Multilayer block copolymer meshes by orthogonal self-assembly. *Nat. Commun.* **7**, 10518 (2016).
8. Tavakkoli K. G., A. *et al.* Templating three-dimensional self-assembled structures in bilayer block copolymer films. *Science* **336**, 1294–1298 (2012).
9. Zhang, L. *et al.* A nanomesh scaffold for supramolecular nanowire optoelectronic devices. *Nat. Nanotechnol.* **11**, 900–906 (2016).
10. Bai, X. *et al.* Room-temperature processing of silver submicron fiber mesh for flexible electronics. *Npj Flex. Electron.* **2**, 3 (2018).
11. Kim, S. Y. *et al.* Large-area nanosquare arrays from shear-aligned block copolymer thin films. *Nano Lett.* **14**, 5698–5705 (2014).
12. Majewski, P. W., Rahman, A., Black, C. T. & Yager, K. G. Arbitrary lattice symmetries via block copolymer nanomeshes. *Nat. Commun.* **6**, 7448 (2015).
13. Liu, R., Huang, H., Sun, Z., Alexander-Katz, A. & Ross, C. A. Metallic nanomeshes fabricated by multimechanism directed self-assembly. *ACS Nano* **15**, 16266–16276 (2021).
14. Cha, S. K. *et al.* Nanopatterns with a square symmetry from an orthogonal lamellar assembly of block copolymers. *ACS Appl. Mater. Interfaces* **11**, 20265–20271 (2019).

15. Subramanian, A., Tiwale, N., Doerk, G., Kisslinger, K. & Nam, C.-Y. Enhanced hybridization and nanopatterning via heated liquid-phase infiltration into self-assembled block copolymer thin films. *ACS Appl. Mater. Interfaces* **12**, 1444–1453 (2020).
16. Jeong, J. W. *et al.* High-resolution nanotransfer printing applicable to diverse surfaces via interface-targeted adhesion switching. *Nat. Commun.* **5**, 5387 (2014).
17. Chu, C. Y. *et al.* Real-space evidence of the equilibrium ordered bicontinuous double diamond structure of a diblock copolymer. *Soft Matter* **11**, 1871–1876 (2015).
18. Chang, C.-Y. *et al.* Mesoscale networks and corresponding transitions from self-assembly of block copolymers. *Proc. Natl. Acad. Sci.* **118**, e2022275118 (2021).
19. Bailey, T. S., Hardy, C. M., Epps, T. H. & Bates, F. S. A noncubic triply periodic network morphology in poly(isoprene-*b*-styrene-*b*-ethylene oxide) triblock copolymers. *Macromolecules* **35**, 7007–7017 (2002).
20. Takenaka, M. *et al.* Orthorhombic *Fddd* network in diblock copolymer melts. *Macromolecules* **40**, 4399–4402 (2007).
21. Epps, T. H. *et al.* Ordered network phases in linear poly(isoprene-*b*-styrene-*b*-ethylene oxide) triblock copolymers. *Macromolecules* **37**, 8325–8341 (2004).
22. Tyler, C. A. & Morse, D. C. Orthorhombic *Fddd* network in triblock and diblock copolymer melts. *Phys. Rev. Lett.* **94**, 208302 (2005).
23. Meuler, A. J., Hillmyer, M. A. & Bates, F. S. Ordered network mesostructures in block polymer materials. *Macromolecules* **42**, 7221–7250 (2009).
24. Bluemle, M. J., Fleury, G., Lodge, T. P. & Bates, F. S. The O^{52} network by molecular design: CECD tetrablock terpolymers. *Soft Matter* **5**, 1587–1590 (2009).
25. Ding, Y. *et al.* Emergent symmetries in block copolymer epitaxy. *Nat. Commun.* **10**, 2974 (2019).
26. Zheng, W. & Wang, Z.-G. Morphology of ABC triblock copolymers. *Macromolecules* **28**, 7215–7223 (1995).
27. Mogi, Y. *et al.* Superlattice structures in morphologies of the ABC triblock copolymers. *Macromolecules* **27**, 6755–6760 (1994).
28. Guo, Z.-H. *et al.* Janus graft block copolymers: Design of a polymer architecture for independently tuned nanostructures and polymer properties. *Angew. Chem. Int. Ed.* **57**, 8493–8497 (2018).
29. Liang, R. *et al.* Hierarchically engineered nanostructures from compositionally anisotropic molecular building blocks. *ChemRxiv* (2022) doi:10.26434/chemrxiv-2022-tn528.
30. Chen, Y. Nanofabrication by electron beam lithography and its applications: A review. *Microelectron. Eng.* **135**, 57–72 (2015).
31. Li, K. *et al.* High speed e-beam writing for large area photonic nanostructures—a choice of parameters. *Sci. Rep.* **6**, 32945 (2016).
32. Sinturel, C., Bates, F. S. & Hillmyer, M. A. High χ–low N block polymers: How far can we go? *ACS Macro Lett.* **4**, 1044–1050 (2015).
33. Jung, Y. S. & Ross, C. A. Orientation-controlled self-assembled nanolithography using a polystyrene−polydimethylsiloxane block copolymer. *Nano Lett.* **7**, 2046–2050 (2007).
34. Gu, W., Hong, S. W. & Russell, T. P. Orienting block copolymer microdomains with block copolymer brushes. *ACS Nano* **6**, 10250–10257 (2012).
35. Gotrik, K. W. *et al.* Morphology control in block copolymer films using mixed solvent vapors. *ACS Nano* **6**, 8052–8059 (2012).
36. Gu, X., Gunkel, I., Hexemer, A., Gu, W. & Russell, T. P. An in situ grazing incidence X-ray scattering study of block copolymer thin films during solvent vapor annealing. *Adv. Mater.* **26**, 273–281 (2014).
37. Lee, S. *et al.* Resolving triblock terpolymer morphologies by vapor-phase infiltration. *Chem. Mater.* **32**, 5309–5316 (2020).
38. Son, J. G., Gotrik, K. W. & Ross, C. A. High-aspect-ratio perpendicular orientation of PS-*b*-PDMS thin films under solvent annealing. *ACS Macro Lett.* **1**, 1279–1284 (2012).
39. Gotrik, K. W. *et al.* 3D TEM tomography of templated bilayer films of block copolymers. *Adv. Funct. Mater.* **24**, 7689–7697 (2014).
40. Huang, H. & Alexander-Katz, A. Dissipative particle dynamics for directed self-assembly of block copolymers. *J. Chem. Phys.* **151**, 154905 (2019).
41. Martínez-Veracoechea, F. J. & Escobedo, F. A. Simulation of the gyroid phase in off-lattice models of pure diblock copolymer melts. *J. Chem. Phys.* **125**, 104907 (2006).
42. F. Hannon, A., Bai, W., Alexander-Katz, A. & A. Ross, C. Simulation methods for solvent vapor annealing of block copolymer thin films. *Soft Matter* **11**, 3794–3805 (2015).

Methods:

Synthesis

The PLA macromonomer[43] $\mathbf{M_{PLA}}$ (M_n = 6.3 kg mol^{-1}) and the PDMS-PS branched macromonomers[5] $\mathbf{M}_y$ (M_n(PDMS) = 5.0 kg mol^{-1}, M_n(PS) = y kg mol^{-1}) used here were synthesized and reported in our previous work. The Grubbs' third generation bispyridyl initiator (G3), $(IMesH_2)(py)_2Cl_2Ru$=CHPh, was synthesized according to literature procedures[44]. All reagents were purchased from commercial suppliers and used without further purification.

Diblock JBBCPs were synthesized by graft-through ROMP according to our previous report[5]. The synthesis of triblock JBBCPs with backbone DPs of m and n, $(PDMS_{5.0\ kg\ mol^{-1}}$-*branch*-$PS_y)_n$-*block*-$(PLA_{6.3\ kg\ mol^{-1}})_m$, was carried out in 2 mL vials equipped with Teflon stir bars. $\mathbf{M_{PLA}}$ (0.030×m μmol) was dissolved in anhydrous dichloromethane (DCM) in the glovebox, followed by addition of the stock solution of G3 in DCM (30 nmol) *via* a micropipette. The total volume of DCM added was ~40 μL. After 0.5 hour, the reaction mixture was first diluted with 20 μL DCM, followed by the addition of the second macromonomer $\mathbf{M}_y$ (0.030×n μmol). The chain was allowed to reinitiate for 5 minutes, and then the reaction mixture was further diluted with 40 μL DCM. After 4 hours' reaction at room temperature, the mixture was removed from the glovebox and quenched with excess ethyl vinyl ether, then dried, characterized, and self-assembled without further purification. A detailed description and discussion as well as a list of the synthesized samples and their characterization are available in the Supplementary Information.

Thin film sample preparation

The JBBCPs were dissolved in chloroform and then spin-coated on either silicon substrates or Si_3N_4 TEM grids (with a 70 nm thick nitride support film acting as the window) to form films with thicknesses ranging from 20 nm to 2 μm. For triblock JBBCP samples, the substrates were surface modified by $\mathbf{M_{PLA}}$, which was spun cast on the substrates, annealed at 130 °C for 24 hours and rinsed with toluene to remove the unreacted material. In this process, the hydroxyl terminal group in $\mathbf{M_{PLA}}$ reacted with the silanol groups at the substrate surface *via* thermally induced dehydration[45], leading to the formation of a PLA surface brush layer.

The thin films were solvent annealed in a closed glass chamber with a solvent reservoir of 2 mL chloroform. The extent of film swelling (S_R) was monitored by spectral reflectometry and was adjusted by nitrogen flow through the chamber with the rate (q_{N_2}) ranging from 3 to 10 sccm controlled by a mass flow controller. The film was quenched by removing the lid of the chamber and taking the sample out of the chamber.

Typically for triblock JBBCPs, the films were first annealed at q_{N_2} = 3 sccm (high S_R) for 30 minutes to anneal the superstructure and then at q_{N_2} = 7 sccm (low S_R) for another 30 minutes to anneal the substructure, unless otherwise stated. For diblock JBBCPs, which do not form superstructures, no significant difference was found with or without the first high-S_R annealing step. The effective volume fractions under this annealing condition are calculated based on the S_R using a modified model from the previous report[42], elaborated in the Supplementary Information.

RIE and SEM imaging

The silicon substrates with JBBCP films were cracked in liquid nitrogen. The cracked edge of one half and the top surface of the other half were reactive ion etched by an 8 s CF_4 plasma (15 mTorr

pressure, 15 sccm gas flow, and 50 W power) to remove the PDMS wetting surface layer and then a 30 s O_2 plasma (6 mTorr pressure, 10 sccm gas flow, and 90 W power) to remove the PS and PLA and oxidize the PDMS microdomains, unless otherwise stated.

For multilayer mesh samples, in addition to the surface morphology, the internal morphology was investigated by angled etching[37] and high-power etching[38]. The terraced regions (Fig. 2c) were obtained by covering the half of the sample, etching the other half with high-power CF_4/O_2 plasma (8 s, 10 mTorr, 10 and 15 sccm gas flow for CF_4 and O_2 respectively, 450 W), removing the cover, further etching the entire sample according to the previous paragraph, and imaging the boundary between these two regions. The morphology in even lower layers could be observed by extending the time of high-power CF_4/O_2 etching or repeating this process.

The etched sample was then imaged using SEM at 3 kV or 5 kV. The cross-sectional view was imaged by tilting the sample by 75°.

STEM imaging and tomography

The STEM samples for top view imaging were made by spin-coating on a nitride substrate and solvent annealing as described above. To avoid the overlapping of multiple mesh layers with different orientations, the film thickness was controlled such that a single-layer mesh was formed. The samples for cross-sectional imaging and the tomography experiments were made by FIB from an unetched thin film sample on a silicon substrate. The unetched sample was first sputter coated with a carbon protection layer of ~40 nm. The thin section specimens were prepared using the lift-out method with a focused Au^+ beam operating at 35 kV and then welded on a copper grid.

STEM imaging and tomography were performed with an aberration-corrected Thermo Fisher Themis Z G3 60–300 kV operated at 200 kV. HAADF images were collected with a 50 pA beam current and a collection angle range of 30–185 mrad. The convergence angle was set to 16 mrad for static images acquisition or 12 mrad for tomography experiments for increased depth of focus. The STEM Tomography program from Thermo Fisher was used for tomography acquisition. Images were collected at each degree of tilt between −45° and 60°. We stopped at −45° because further increasing the tilting magnitude caused one end of the sample membrane to block the beam. 3D reconstruction of tomography data was carried out by the algebraic reconstruction technique (ART).

DPD Simulation

The simulations were carried out using the LAMMPS package[46] with GPU acceleration[47]. All simulations represent a canonical (*NVT*) ensemble, and all quantities are unitless in the model, with the fundamental quantities such as mass, distance, and thermal energy k_BT set to unity. DPD is a coarse-graining particle-based simulation technique, which overcomes the time- and space-scale limitation encountered in molecular dynamics simulations and is powerful in tracking the morphology evolution[48]. The triblock copolymer is modeled as a series of beads representing the sidechains and the backbone, connected by linear harmonic bonds. We fixed the backbone beads number in the homo-C domain and the branched A-B domain to be $m = n = 20$ and the number of the C branch beads $N_C = 10$, and we varied the number of A and B branch beads ((N_A, N_B) = (3, 7), (4, 8), (4, 7), (4, 6), or (6, 6)) to tune the volume fractions (f_A' = 30%, 33%, 36%, 40%, or 50%). The time evolution of the beads is governed by Newtonian motion due to conservative, dissipative, and random forces, all of which are pairwise-additive, short-range, and cut at $r_0 = 1.0$. In the reparametrized model[40] we used, the bead density was set to be $\rho = 5$, the repulsion parameter for the same bead type $a_{ii} = 15$, and the harmonic bond potential was set with the spring constant K^B =

50 and equilibrium distance r_0 = 1.0. To qualitatively mimic the immiscibility between different types of monomers in this system, we set repulsion parameters $a_{AB} = 22.5$ and $a_{AC} = a_{BC}$ = 26.0 unless otherwise stated. The relationship between the repulsion parameters and the Flory–Huggins parameter χ between two different beads is defined by equation $a_{ij} \approx a_{ii} + 1.45\,\chi_{ij}$. No interaction was set between backbone beads and side chain beads; thus, the backbone beads were not included in the calculation of the volume fractions. To qualitatively mimic the stiffness of bonds in the backbone, a square angle potential between two adjacent bonds was applied, $V^A = K^A(\theta - \theta_0)^2$, where K^A is the potential constant, θ is the angle between two neighboring bonds, and the equilibrium angle θ_0 was set to be π. Since the stiffness is dependent on the grafting density[29], we set $K^A = 1$ for the homo-C domain backbone and $K^A = 2$ for the branched A-B domain backbone.

The noise parameter σ was set to be 3.0 for the initial 800 000 premixing steps and was then reduced to 0.1 for the remaining 12 000 000 steps to find the stable morphology in the *NVT* system. Around 10% solvent beads that are neutral to all types of beads were added to the system to improve the mobility of JBBCPs and avoid formation of potential trapped metastable states[13]. For the simulation of diblock JBBCPs, we set a cubic simulation box with dimensions $L_x = L_y = L_z = 13$; for triblocks, tetragonal boxes were used with an in-plane size of $L_x = L_z = 13$, and the height $L_y = 24$ or 46 was set to be commensurate with 1 or 2 layers of LAM superstructure. Periodic boundary conditions were applied in all three directions for all simulations. More details of the DPD setup are described in the Supplementary Information.

References for Methods:

43. Vohidov, F. *et al.* ABC triblock bottlebrush copolymer-based injectable hydrogels: design, synthesis, and application to expanding the therapeutic index of cancer immunochemotherapy. *Chem. Sci.* **11**, 5974–5986 (2020).
44. Sanford, M. S., Love, J. A. & Grubbs, R. H. A versatile precursor for the synthesis of new ruthenium olefin metathesis catalysts. *Organometallics* **20**, 5314–5318 (2001).
45. Edwards, E. W., Montague, M. F., Solak, H. H., Hawker, C. J. & Nealey, P. F. Precise control over molecular dimensions of block-copolymer domains using the interfacial energy of chemically nanopatterned substrates. *Advanced Materials* **16**, 1315–1319 (2004).
46. Thompson, A. P. *et al.* LAMMPS – A flexible simulation tool for particle-based materials modeling at the atomic, meso, and continuum scales, *Comp. Phys. Comm.* **271**, 108171 (2022).
47. Brown, W. M., Wang, P., Plimpton, S. J. & Tharrington, A. N. Implementing molecular dynamics on hybrid high performance computers – short range forces. *Comput. Phys. Commun.* **182**, 898–911 (2011).
48. Hoogerbrugge, P. J. & Koelman, J. M. V. A. Simulating microscopic hydrodynamic phenomena with dissipative particle dynamics. *EPL* **19**, 155–160 (1992).

Acknowledgements:

J.A.J. acknowledges support from Eni S.p.A. through the MIT Energy Initiative. C.A.R. acknowledges support from NSF DMREF award 2118678. M.Z. acknowledges support from the NSF DMR award 2003875. This work was carried out in part through the use of MIT.nano's facilities and APS, a U.S. DOE Office of Science User Facility operated for the DOE Office of Science by Argonne National Laboratory (Contract No. DE-AC02-06CH11357). Shared facilities of CMSE, NSL, and MRSEC under award DMR1419807 were used. The authors acknowledge the MIT Satori, the MIT SuperCloud, MIT Research Computing Project, and Lincoln Laboratory Supercomputing Center for providing HPC resources that have contributed to the research results reported here. The authors thank Eunsoo Cho and Dr. Aubrey Penn for the help on STEM imaging and Yifu Ouyang for helpful discussion.

Author contributions:

Z. S., K. K., and B. L. synthesized the JBBCPs. Z. S., R. Liu, and T. S. prepared the samples. Z. S., R. Liu, T. S., and R. Liang conducted structure and property characterization. Z. S., R. Liu, H. H., and A. A.-K. conducted the simulations. Z. S., R. Liu, M. Z., C. A. R., and J. A. J. conceived of the idea. Z. S., C. A. R., and J. A. J. wrote the manuscript.

Figs. 1–4 with captions: See below.

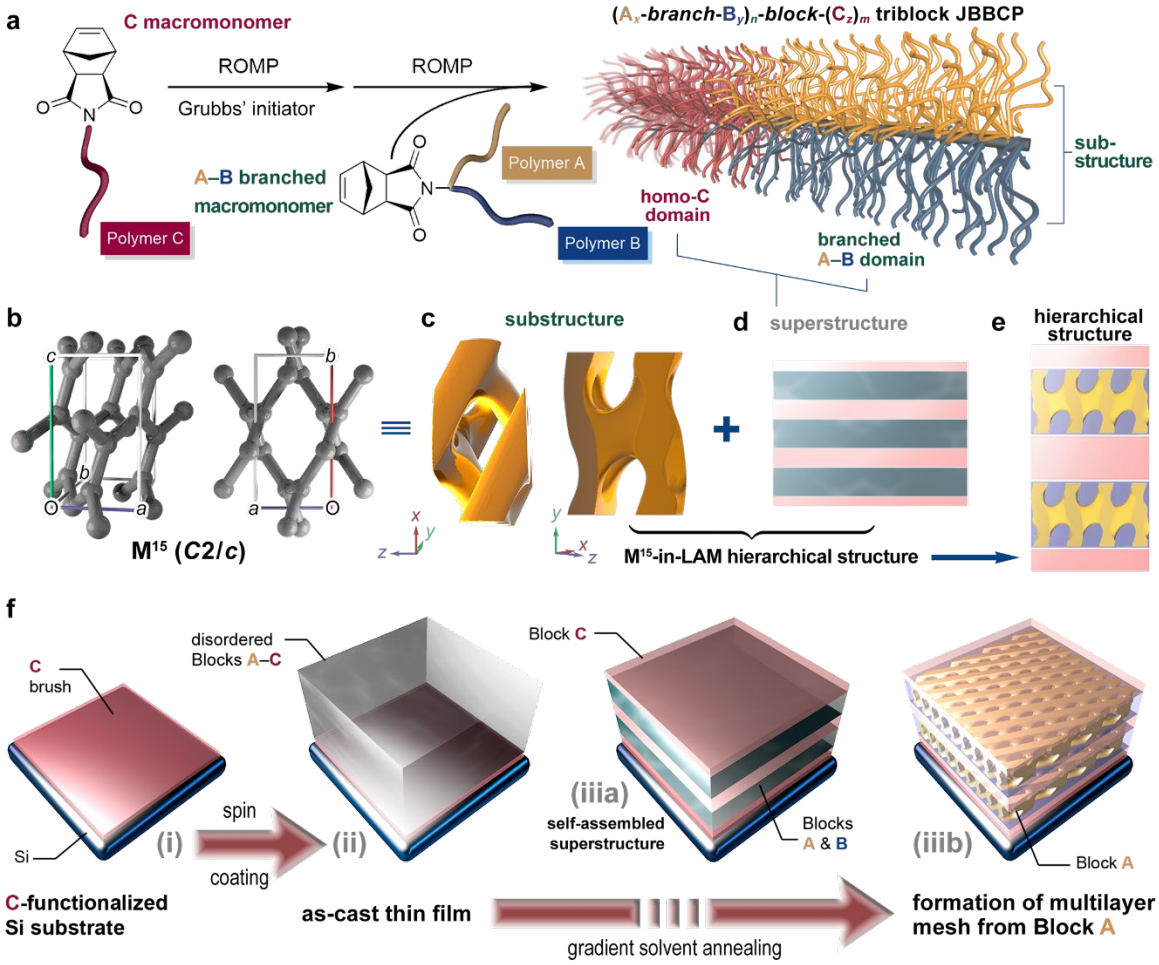

Fig. 1. Fabrication of multilayer nanomeshes based on intrinsic molecular confinement self-assembly of the triblock JBBCPs. a, The synthetic scheme for the triblock JBBCPs. **b,** The ball-and-stick model and **c,** the mathematical space-filling model for a M^{15} network in a unit cell. The formation of the M^{15} substructure is driven by the intrinsic molecular confinement from **d,** the LAM superstructure. **e,** The M^{15}-in-LAM hierarchical structure formed by the combination of the superstructure and substructure from the self-assembled triblock JBBCP. **f,** Schematic illustration of the fabrication procedures for the multilayer nanomeshes.

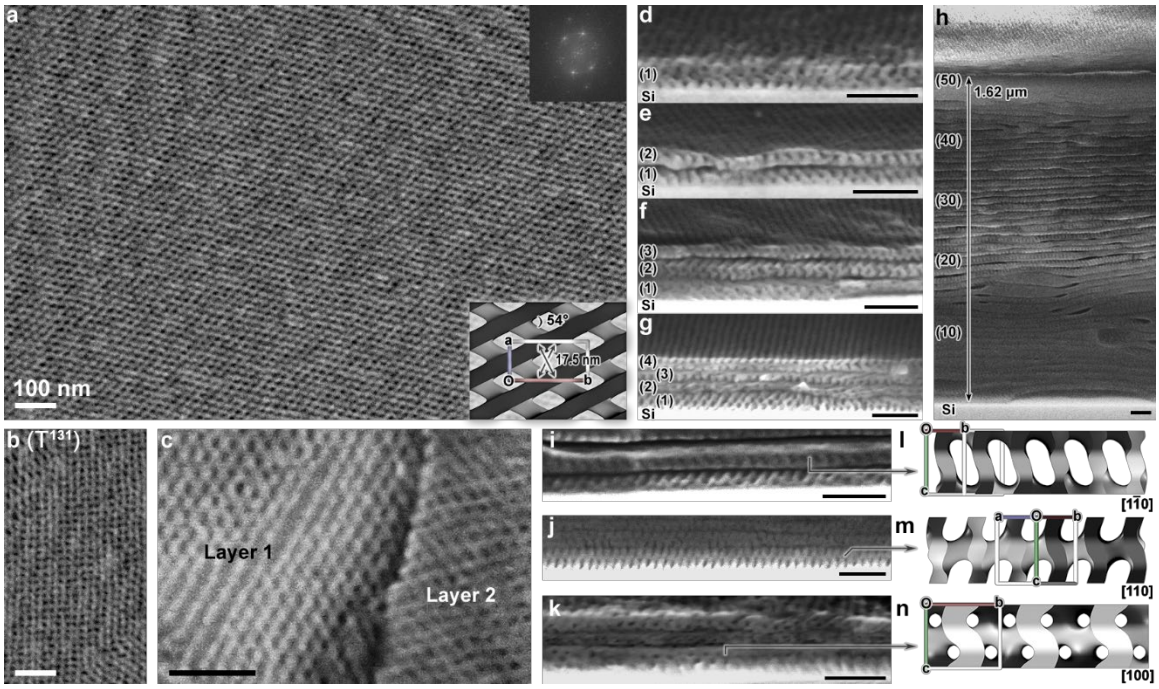

Fig. 2. SEM imaging of the multilayer nanomesh structures. a, Top view of a micron-scale long-range ordered 54° mesh network with an inter-line spacing of 17.5 nm (inset on the top right: FFT). Its full-scale image is shown in Supplementary Fig. 21. The other inset is the top projection of a mathematical model for the M^{15} network shown at higher magnification. **b,** Top view of a coexistent 90° mesh network with the same inter-line spacing, taking up 2% of the total area (full-scale image shown in Supplementary Fig. 21). **c,** Top view of the terraced region after angled etch, showing the mesh networks in two different layers, which exhibit no interlayer correlation. **d–h,** Cross-sectional views of single-, 2-, 3-, and 4-layer nanomeshes, fabricated by thin films of different thicknesses. **i–k,** Cross-sectional views of the nanomeshes, showing features in agreement with **l–n,** [1$\bar{1}$0], [110], and [100] projections of the M^{15} model. All pictures were from the self-assembly of $\mathbf{T6.9_{30\text{-}30}}$ thin films after RIE, showing bright A blocks (*i.e.*, oxidized PDMS), and all scale bars are 100 nm.

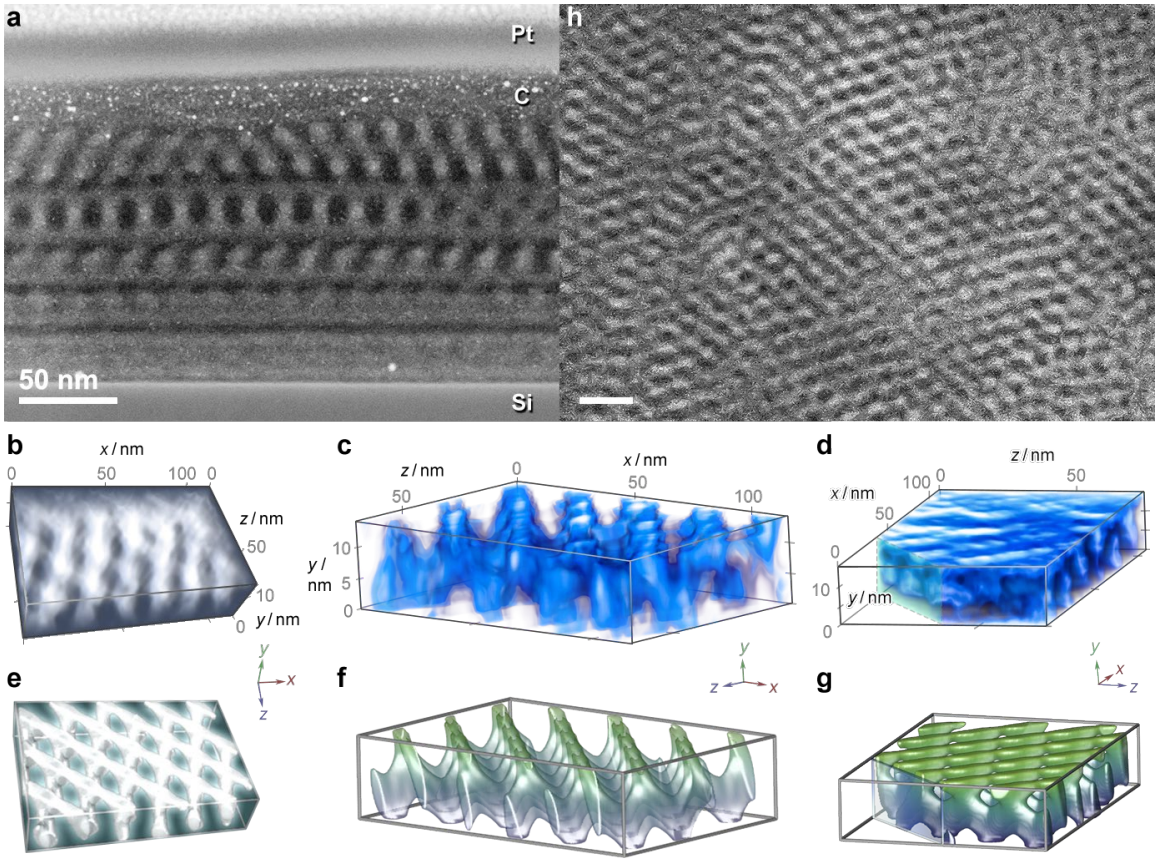

Fig. 3. STEM imaging and tomography evidence for the M^{15} substructure. a, STEM imaging of an unetched, FIB-cross-sectioned **$T6.9_{30\text{-}30}$** thin film sample. **b–d,** Volume rendering of the 3D tomography reconstruction for the substructure network from the same sample as in **a**. **e–g,** Mathematical model for the M^{15} network viewed from the same angles as **b–d**. **h,** The STEM plain view of unetched single-layer nanomeshes fabricated from **$T6.9_{30\text{-}30}$** on a silicon nitride membrane substrate. The scale bars are 50 nm.

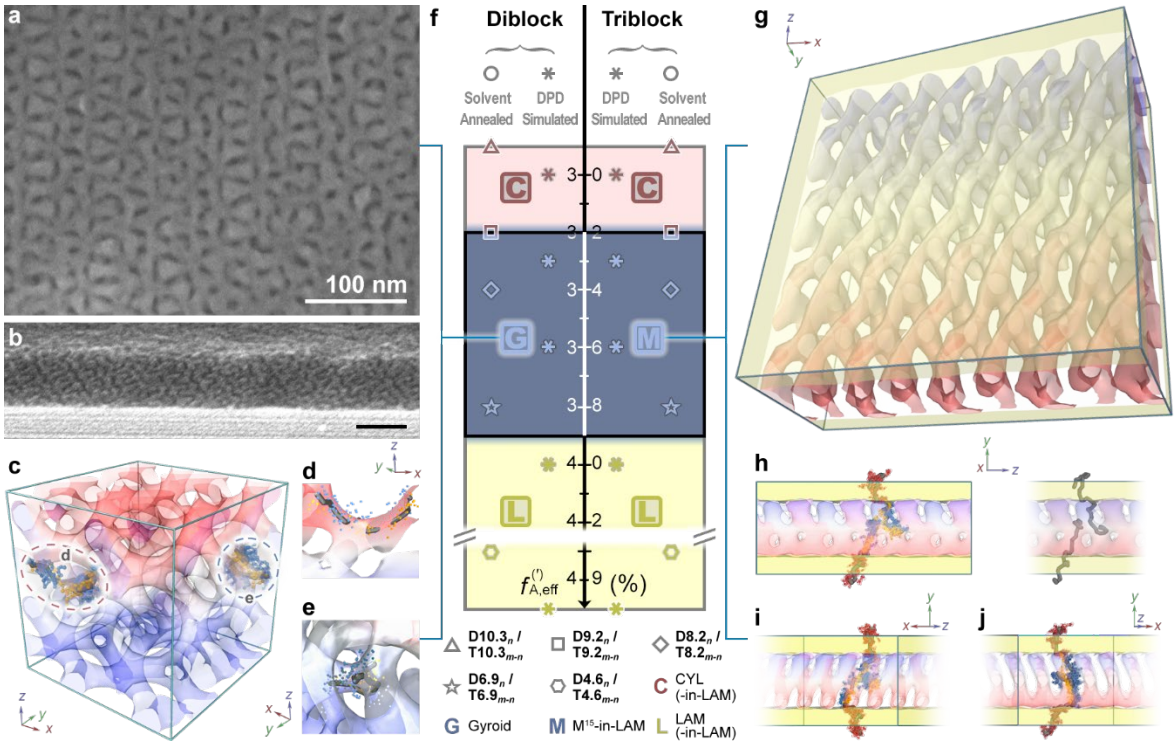

Fig. 4. Comparison of the networks and the phase diagrams between di- and triblock JBBCPs. a–b, Top and cross-sectional SEM images of the GYR-forming **D6.9$_{30}$** thin film. The scale bars are 100 nm. **c–e,** DPD simulated GYR structure for a diblock JBBCP with f_A = 33%. **d,** The strut-forming backbones are extended. **e,** The node-forming backbones are coiled. **f,** Experimental and simulated phase diagrams for di- and triblock JBBCPs, showing a one-to-one mapping relationship. Especially, the phase region of the M^{15} network substructure matches well with that of GYR. The morphology of each data point is shown in Supplementary Fig. 36–42. **g–j,** DPD simulated M^{15}-in-LAM structure for a triblock JBBCP with $f_A' = 33\%$, showing extended backbones. **h–j** display the [100], [110], and [1$\bar{1}$0] projections of the M^{15} network, respectively.